Chemical Science

ROYAL SOCIETY OF CHEMISTRY

EDGE ARTICLE

View Article Online
View Journal | View Issue

Cite this: *Chem. Sci.*, 2021, **12**, 718

All publication charges for this article have been paid for by the Royal Society of Chemistry

Understanding the unique reactivity patterns of nickel/JoSPOphos manifold in the nickel-catalyzed enantioselective C–H cyclization of imidazoles†

Jian-Biao Liu, *[a] Xin Wang,[a] Antonis M. Messinis, [b] Xiao-Jun Liu, [a] Rositha Kuniyil,[b] De-Zhan Chen *[a] and Lutz Ackermann *[b]

Received 19th August 2020
Accepted 31st October 2020

DOI: 10.1039/d0sc04578k

rsc.li/chemical-science

The 3d transition metal-catalyzed enantioselective C–H functionalization provides a sustainable strategy for the construction of chiral molecules. A better understanding of the catalytic nature of the reactions and the factors controlling the enantioselectivity is important for rational design of more efficient systems. Herein, the mechanisms of Ni-catalyzed enantioselective C–H cyclization of imidazoles are investigated by density functional theory (DFT) calculations. Both the π-allyl nickel(II)-promoted σ-complex-assisted metathesis (σ-CAM) and the nickel(0)-catalyzed oxidative addition (OA) mechanisms are disfavored. In addition to the typically proposed ligand-to-ligand hydrogen transfer (LLHT) mechanism, the reaction can also proceed *via* an unconventional σ-CAM mechanism that involves hydrogen transfer from the JoSPOphos ligand to the alkene through P–H oxidative addition/migratory insertion, C(sp^2)–H activation *via* σ-CAM, and C–C reductive elimination. Importantly, computational results based on this new mechanism can indeed reproduce the experimentally observed enantioselectivities. Further, the catalytic activity of the π-allyl nickel(II) complex can be rationalized by the regeneration of the active nickel(0) catalyst *via* a stepwise hydrogen transfer, which was confirmed by experimental studies. The calculations reveal several significant roles of the secondary phosphine oxide (SPO) unit in JoSPOphos during the reaction. The improved mechanistic understanding will enable design of novel enantioselective C–H transformations.

Introduction

The selective C–H functionalization has emerged as one of the most practical and powerful tools in molecular syntheses.[1] Although major progress has been realized using the second and third row transition metals, recent developments have enabled many promising transformations that employ earth-abundant and less toxic 3d metals.[2] In this context, nickel catalysts exhibit several unique properties[3] and have served as an efficient alternative approach in a wide range of catalytic processes in the past few years.[2b] However, despite nickel being widely applied in numerous reactions, Ni-catalyzed enantioselective C–H activations have been rarely reported.[4] The reactivity of nickel catalysts is highly sensitive to the substrates and ligands in most cases, resulting in narrow substrate scope and limited choices of viable chiral ligands.

Imidazole derivatives are among the most significant heterocyclic structural moieties present in a broad variety of biologically active compounds.[5] The construction and modification of imidazole derivatives, especially synthesis of imidazole compounds bearing stereocenters, are consequently of great interest and importance. In 2018, Ye and coworkers reported the enantioselective C–H cyclization of imidazoles with alkenes employing the Ni–Al bimetallic catalysis (Scheme 1a).[6] A screening of a variety of chiral ligands indicated that the bis(*t*-butyl)phenyl-containing TADDOL-derived secondary phosphine oxide (SPO) ligand TADDOL–SPO was the optimal one. The TADDOL–SPO ligand enables the synthesis of polycyclic imidazoles with exclusive *exo*-selectivity and high enantiomeric excesses. In a very recent example, we reported a complementary approach that enables *endo*-selective hydroarylation of unactivated alkenes in the absence of organoaluminum reagents (Scheme 1b).[7] Essential to the success of this reaction is the use of bidentate JoSPOphos ligand (**L**), whose applications were previously restricted to rhodium(I)-catalyzed hydrofunctionalizations.[8] This simple catalytic system allows the synthesis of imidazole products containing chiral six-membered ring with high enantioselectivities.

[a]*College of Chemistry, Chemical Engineering and Materials Science, Shandong Normal University, Jinan 250014, China. E-mail: jianbiaoliu.thu@gmail.com; chendzh@sdnu.edu.cn*

[b]*Institut für Organische und Biomolekulare Chemie, Georg-August-Universität Göttingen, Göttingen 37077, Germany. E-mail: Lutz.Ackermann@chemie.uni-goettingen.de*

† Electronic supplementary information (ESI) available: Additional computational and experimental results, calculated energies and imaginary frequencies, and Cartesian coordinates of optimized structures. See DOI: 10.1039/d0sc04578k

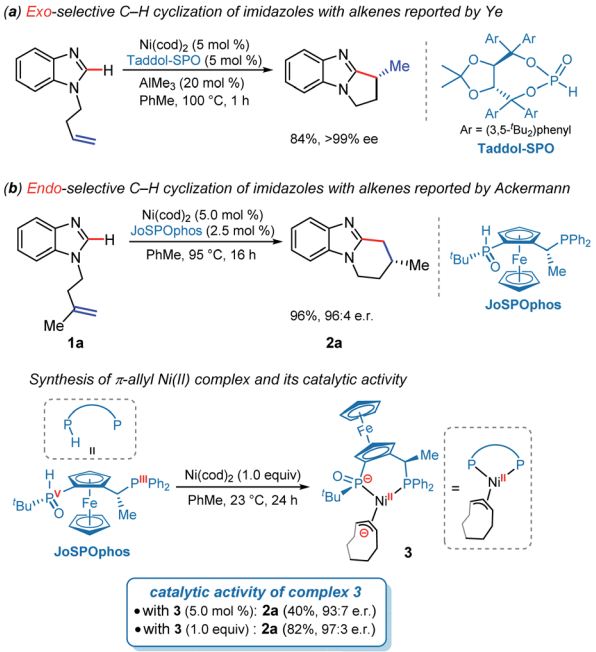

Scheme 1 Ni-catalyzed intramolecular enantioselective C–H cyclization of imidazoles.

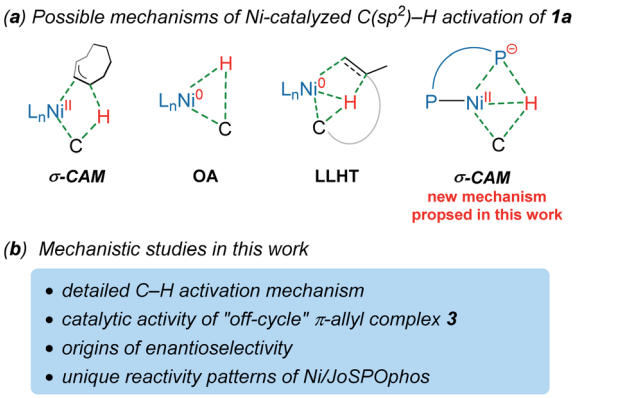

Scheme 2 The plausible mechanisms of the Ni-catalyzed C(sp^2)–H activation of **1a** and mechanistic studies in this work.

Understanding the detailed mechanisms of Ni-catalyzed C–H functionalizations could guide the design of catalysts and the control of selectivity. However, the existing ligand exchanges and the potential of off-cycle intermediates lead to considerable complexities. To provide insights into the mechanism of the reaction in Scheme 1b, a well-defined η^3–π-allyl nickel(II) complex **3** was isolated and tested for catalytic activity.[7] This stable π-allyl nickel(II) complex was generated from pre-catalyst Ni(cod)$_2$ (cod = 1,5-cyclooctadiene) and JoSPOphos *via* classical Ni-mediated chain-walking mechanism.[9] Interestingly, complex **3** was found to be catalytically active in the enantioselective intramolecular alkylation of *N*-allylic benzimidazole **1a**. Previous reports by Zimmerman and Montgomery have shown that the π-allyl complex is actually an off-cycle intermediate and its formation can drastically inhibit catalysis in the *N*-heterocyclic carbene–nickel-catalyzed hydroarylation.[10] The experimentally observed reactivity of the π-allyl nickel(II) complex reported by us remains elusive.

Although the mechanism and selectivity of transition-metal-catalyzed hydroarylation of alkenes has been reported by several computational studies,[11] the precise mode of C(sp^2)–H activation[12] and the origins of enantioselectivity remain unclear for the nickel/JoSPOphos system (Scheme 2). Herein, we report a detailed mechanistic study on the titled reaction by means of density functional theory (DFT) calculations. Our calculations show that both the nickel(II)-promoted σ-complex-assisted metathesis (σ-CAM)[13] and the nickel(0)-catalyzed oxidative addition (OA) mechanisms are disfavored. Besides the common nickel(0)-catalyzed ligand-to-ligand hydrogen transfer (LLHT) mechanism,[14] an unconventional nickel(0)-catalyzed σ-CAM mechanism is found to be also viable. The experimentally observed catalytic activity of π-allyl nickel(II) complex **3** can be rationalized by the regeneration of the nickel(0) complex *via* a stepwise hydrogen transfer from cod-derived π-allyl ligand to JoSPOphos, which subsequently promotes the nickel(0)/nickel(II) catalytic cycle. This new mechanistic scenario provides new insights into the unique reactivity patterns of the nickel/JoSPOphos catalytic system and new guidelines for future design of other asymmetric C–H transformation.

Computational details

Geometry optimizations were performed in solvent (toluene) at the B3LYP[15]-D3(BJ)[16]/6-31G(d,p)/LANL2DZ(Ni)[17] level of theory with the corresponding effective core potential (ECP) on Ni. This computational method has been successfully applied to investigate various Ni-catalyzed C–H functionalizations.[18] Frequency calculations were performed at the same theoretical level to verify the nature of the stationary points and to obtain the thermal Gibbs free energy corrections at 368.15 K. A correction to the harmonic oscillator approximation, as proposed by Grimme,[19] was applied during the entropy calculations with a frequency cut-off of 50 cm^{-1}. Considering the entropy in the solution phase is inadequately described due to the suppression of translational entropy upon moving from the gas phase to the solvent, the translational entropy in solution was estimated by the method of Whitesides.[20] All the entropy corrections were finished by using the Goodvibes program.[21] Intrinsic reaction coordinate (IRC) calculations were carried out to confirm that each transition state connected the corresponding reactant and product. To obtain more accurate electronic energies, single point calculations at B3LYP-D3(BJ)/def2-TZVP[22] were carried out in the solvent. The continuum solvation model SMD[23] was utilized to consider the bulk solvent effects. The correction caused by the different standard states in the gas phase and in solution was added to the free energies of all species.

All the DFT calculations were conducted with the Gaussian 09 software.[24] The natural population analysis (NPA) and localized orbital locator (LOL) analysis were performed by GenNBO 5.0 (ref. 25) and Multiwfn 3.6 (ref. 26) respectively, using the wavefunction obtained from B3LYP-D3(BJ)/6-

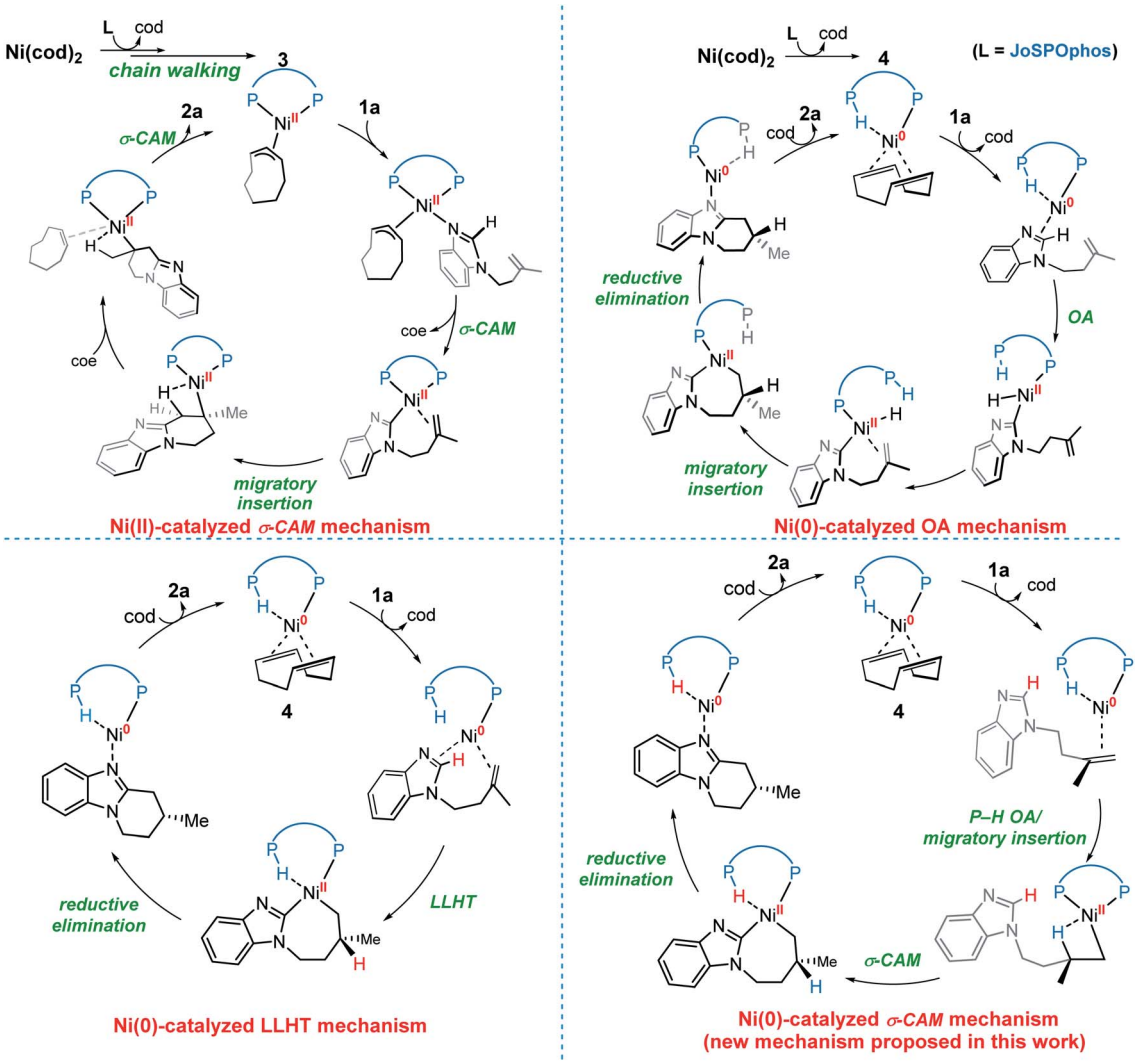

Scheme 3 The four possible mechanisms of the Ni-catalyzed enantioselective C–H cyclization of imidazoles.

31G(d,p)/LANL2DZ(Ni) level. The 3D diagrams of molecules were prepared by CYLview.[27]

Results and discussion

The four possible catalytic cycles

On the basis of previous investigations[7,11] and our calculations, there are four plausible mechanisms of the Ni-catalyzed enantioselective C–H cyclization of imidazoles. As shown in Scheme 3, the σ-CAM mechanism, starting from the π-allyl nickel(II) complex **3**, involves C(sp^2)–H cleavage *via* σ-complex-assisted metathesis, migratory insertion and the second σ-complex-assisted metathesis. The OA mechanism starts from the nickel(0) complex **4** and proceeds *via* C(sp^2)–H oxidative addition, migratory insertion and C–C reductive elimination to afford the final product and regenerate the active nickel(0) catalyst. The LLHT mechanism consists of C(sp^2)–H activation *via* direct ligand-to-ligand hydrogen transfer from the imidazole to the alkene and the subsequent reductive elimination. This LLHT mechanism, originally proposed by Eisenstein and Perutz for hydrofluoroarylation of alkynes with Ni catalysts,[14] is the more commonly proposed mechanism for Ni-catalyzed hydroarylation. Another unconventional σ-CAM mechanism, involving stepwise hydrogen transfer from JoSPOphos ligand to the alkene *via* P–H oxidative addition/migratory insertion, C(sp^2)–H activation *via* σ-complex-assisted metathesis and reductive elimination, is proposed in this work.

Nickel(II)-catalyzed σ-CAM mechanism

We first investigated a catalytic cycle initiated by the π-allyl nickel(II) complex **3**. The free energy profile for the nickel(II)-promoted hydroarylation is depicted in Fig. 1. All energies are presented with respect to complex **4**, which is formed by ligand exchange of the precatalyst $Ni(cod)_2$ with **L**. In complex **4**, the bidentantate JoSPOphos ligand coordinates with the metal *via* the lone pair of the P(III) atom and the P(V)–H bond respectively. This complex is 3.1 kcal mol^{-1} more stable than the corresponding *O*-coordinated analog (see Scheme S1 and Table S1 in the ESI† for more details). We also considered the tautomeric

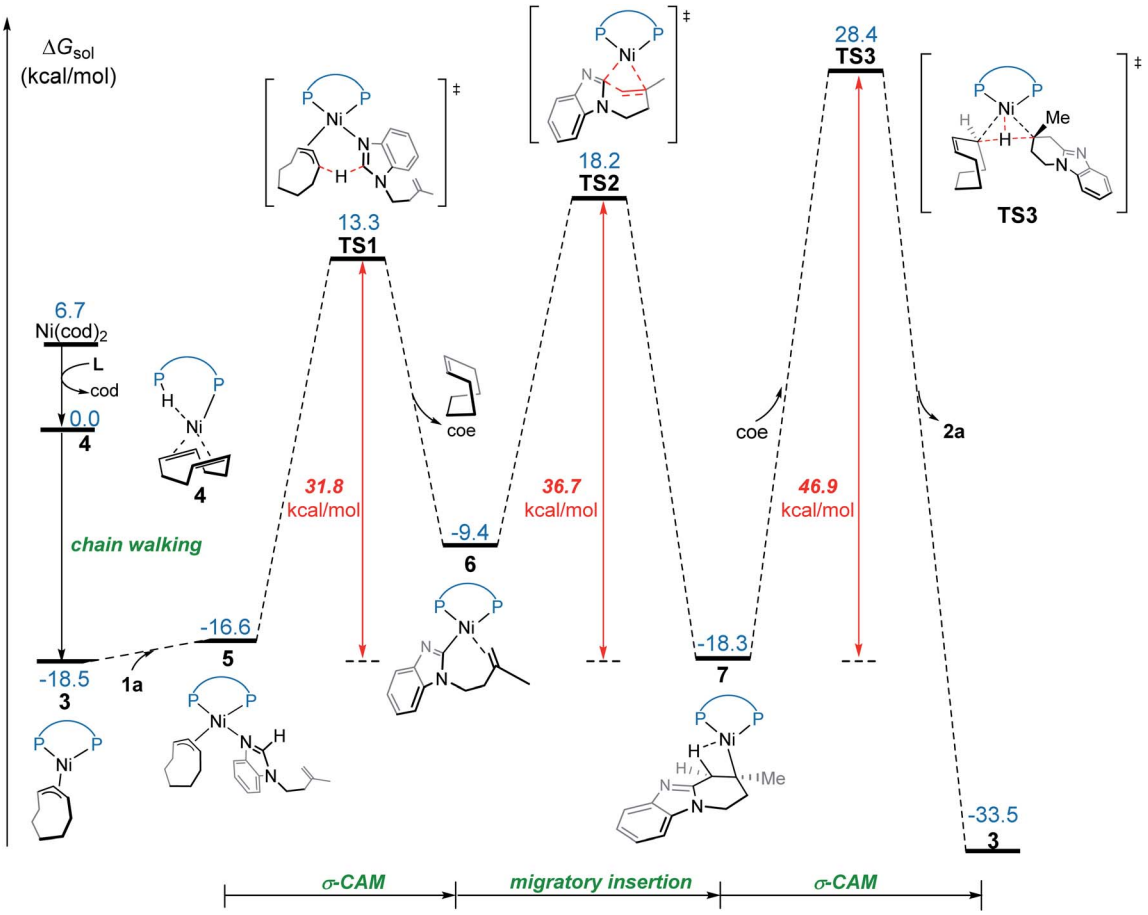

Fig. 1 Free energy profile for nickel(II)-promoted hydroarylation *via* the σ-CAM mechanism.

equilibrium between the pentavalent phosphine oxide and the trivalent phosphinous acid.[28] However, the tautomeric conversion is kinetically unfavorable for the JoSPOphos ligand (see Scheme S1 and Fig. S1 in the ESI†). For complex **4**, the P–H bond becomes slightly longer by 0.04 Å after the formation of the agostic interaction. The agostic interaction between P–H with nickel(0) is further confirmed by Bader's atoms in molecules (AIM) analysis,[29] which shows there exists a bond critical point between Ni and H atoms (Fig. 2). To the best of our knowledge, this kind of binding mode of JoSPOphos ligand has not been explored previously.

Complex **4** then undergoes facile P–H oxidative addition along with migratory insertion to form a nickel(II) intermediate, from which the traditional chain walking involving consecutive β-hydride elimination/migratory insertion occurs to yield the π-allyl nickel(II) complex **3** (Fig. S2 and S3 in the ESI†). As compared to the precatalyst $Ni(cod)_2$, complex **3** is 25.2 kcal mol^{-1} more stable, explaining why it can thus be isolated in the experiment.[7]

From complex **3**, coordination of the substrate **1a** *via* N atom forms the four-coordinate complex **5**. The subsequent σ-complex-assisted metathesis step with π-allyl as the base (**TS1**; see Fig. 3 for the optimized structure) requires 31.8 kcal mol^{-1}, relative to **3**. In the resulting deprotonated intermediate **6**, the olefin moiety of the substrate is coordinated with the metal center to get prepared for the following cyclization. The olefin migratory insertion into the newly formed Ni–C bond takes place *via* four-membered transition state **TS2**, with a much higher barrier relative to **3**.

To complete the catalytic cycle, protonation is required for the cyclized intermediate **7** to liberate the final product. The corresponding $C(sp^3)$–H bond cleavage occurs *via* σ-CAM

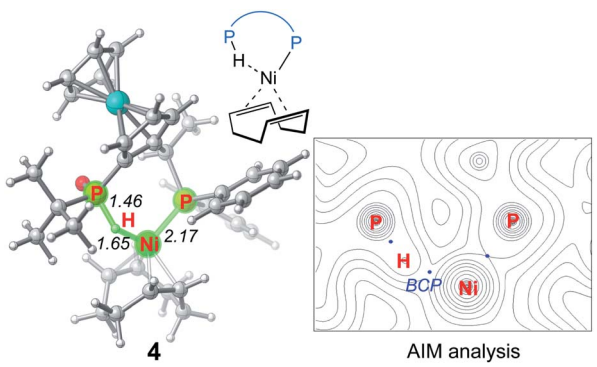

Fig. 2 Optimized structure of **4** with selected bond distances in Å and corresponding AIM analysis.

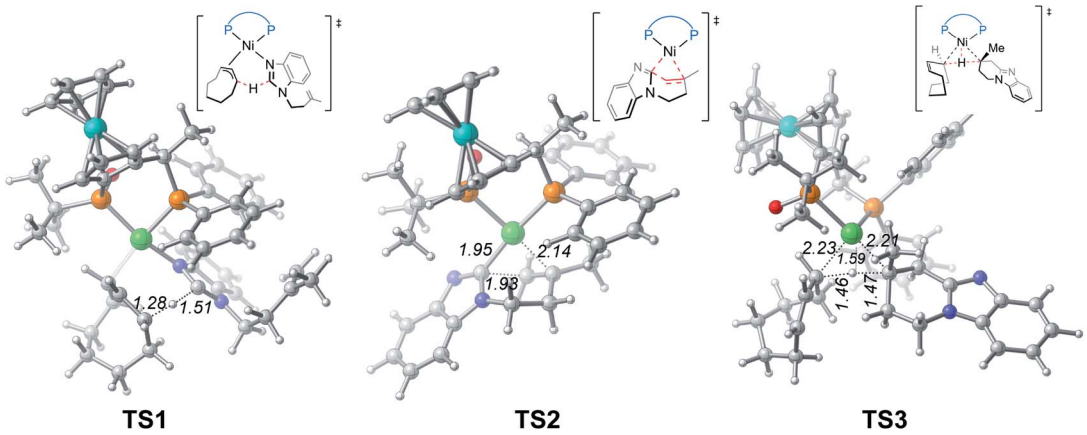

Fig. 3 Optimized structures of transition states **TS1**, **TS2** and **TS3** with selected bond distances in Å.

transition state **TS3**, in which the proton is transferred from cyclooctene (COE) to the cyclized moiety. However, the σ-CAM process is highly disfavored due to the significantly higher barrier (**TS3**, $\Delta G^{\ddagger} = 46.9$ kcal mol^{-1} relative to **3**). We also considered the proton abstraction from an additional substrate **1a**, but the corresponding transition state is even higher in energy (see **TS3′** in Fig. S4†). Overall, our calculations highlight that, while the step of σ-CAM C(sp^2)–H activation is operative, this reaction pathway is kinetically unfavorable due to the considerably higher barrier of the succeeding steps, especially the second σ-CAM. The experimentally observed catalytic activity of nickel(II) complex **3** will be discussed later.

Nickel(0)-catalyzed OA mechanism

From complex **4**, the substrate-ligand exchange with **1a** can form several different substrate-coordinated complexes *via* either *N*- or alkene-coordination. As shown in Fig. 4, for the *mono*-imidazole complexes, the formations of η^2-alkene coordination complex **c1** and the N-coordinate complex **c2** from **4** are endergonic by 2.3 and 7.2 kcal mol^{-1}, respectively. Further coordination of the substrates results in various bisligated complexes, among which the Y-shape complex **c3** is the most energetically favorable one. All the possible substrate-coordinated complexes are compared in Fig. S7 and Table S2 in the ESI.†

In the OA mechanism, dissociation of one substrate from catalyst **c3** occurs first to generate intermediate **8**, which is endergonic by 17.7 kcal mol^{-1} (Fig. 5). The C(sp^2)–H oxidative addition then occurs *via* a three-membered transition state **TS4**, which requires a relatively higher barrier of 33.1 kcal mol^{-1}. Subsequently, the resulting nickel hydride **9** undergoes consecutive isomerization to generate the η^2-alkene coordination complex **11**. This complex (**11**) undergoes migratory insertion *via* **TS5** to form the nickelacycle intermediate **12**. The migratory insertion might also occur with intermediate 10, but this alternative reaction pathway (**TS5′** in Fig. S8†) is less favorable as compared to **TS5**, probably due to the absence of agostic interaction. Intermediate **12** subsequently undergoes C–C reductive elimination *via* **TS6** to afford the product-coordinated complex **13**. Product liberation of complex **13** releases the *endo*-product and regenerates the active catalyst **c3**. In the OA mechanism, the migratory insertion requires an activation free energy of 36.7 kcal mol^{-1} with respect to **c3**, which indicates this mechanism is infeasible under the experimental conditions.

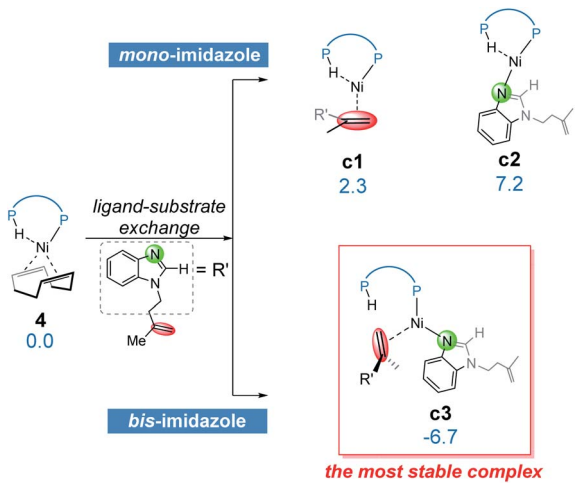

Fig. 4 The possible ligand-substrate exchanges and representative substrate-coordinated complexes with energies in kcal mol^{-1}.

Nickel(0)-catalyzed LLHT mechanism

In the LLHT mechanism, the formation of the alkene-coordinated complex **c7** from **c3** is 14.7 kcal mol^{-1} endergonic (Fig. 6). In the three-coordinate complex **c7**, the C(sp^2)–H bond becomes closer to the metal center and the agostic interaction between P–H with nickel(0) cannot be formed due to the steric repulsions between SPO and the benzoimidazolyl moiety in the substrate. Complex **c7** then undergoes LLHT *via* **TS7**,[30,31] in which the oxidative addition of the C(sp^2)–H bond is coupled with migratory insertion. The preference for LLHT mechanism for nickel catalyst can be attributed to the relatively small atomic radius of nickel and weak Ni(II)–H bond. To

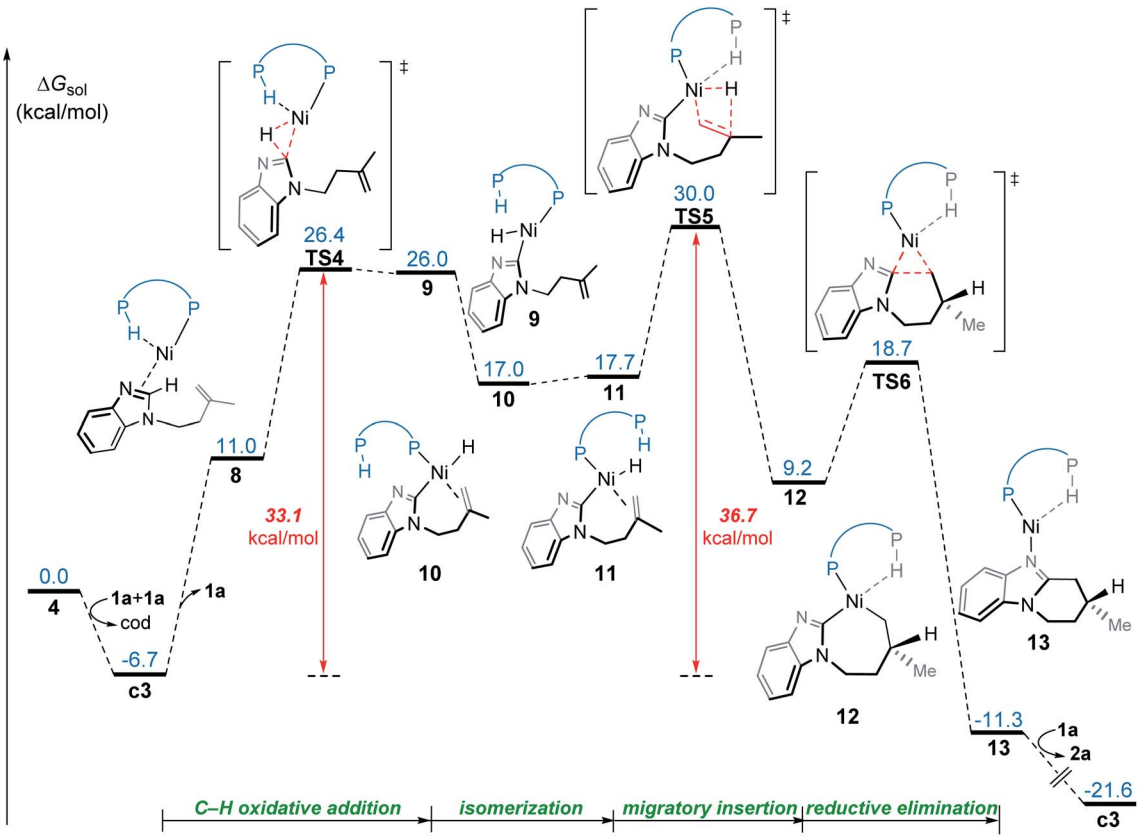

Fig. 5 Free energy profile for nickel(0)-promoted hydroarylation *via* the OA mechanism.

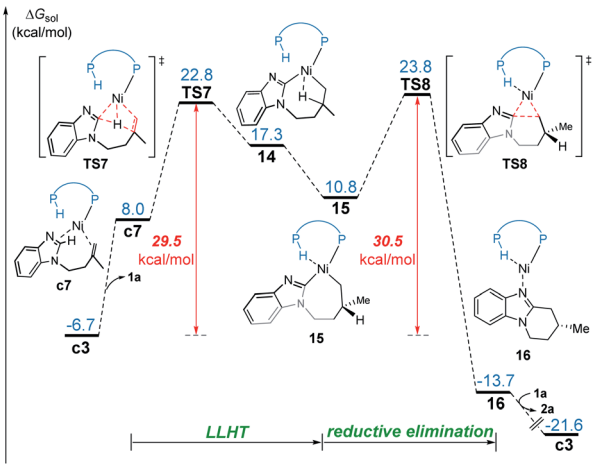

Fig. 6 Free energy profile for nickel(0)-promoted hydroarylation *via* the LLHT mechanism.

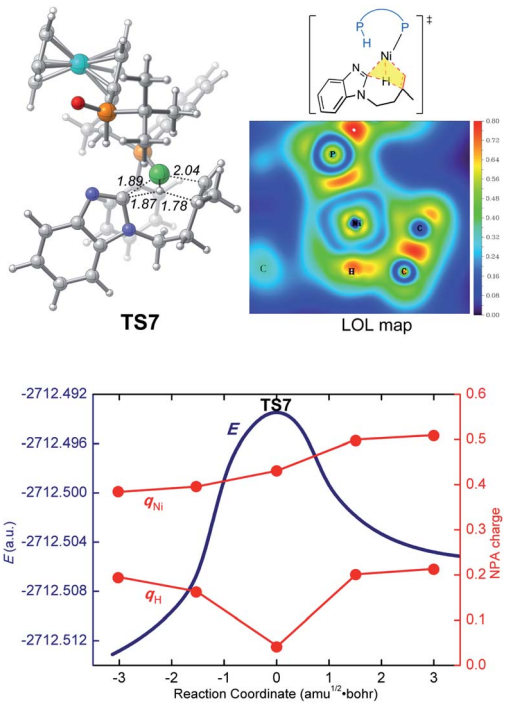

Fig. 7 Optimized structure of the LLHT transition state **TS7** with selected bond distances in Å, the LOL map, and the electronic energies (*E*) and NPA charges (*q*) along the intrinsic reaction coordinates.

further investigate electronic structures of the transition state **TS7**, we performed additional NPA and LOL calculations. The LOL map in Fig. 7 clearly reveals that, although the Ni–H distance is relatively short at the transition state, the electron is localized around the migrating hydrogen instead of the middle regions between Ni and H atoms. The LOL picture is consistent with the calculated NPA charge of the transferring charge of H; the charge of H decreases significantly at the first-order saddle

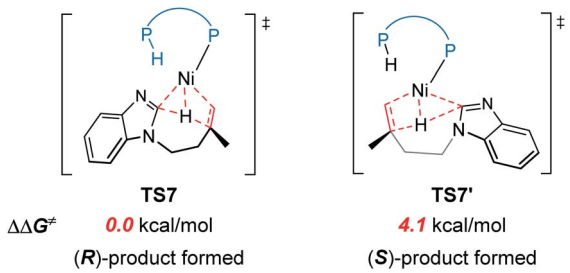

Fig. 8 A comparison of the two competing LLHT transition states TS7and TS7′.

point.[32] During the LLHT process, the NPA charge of Ni gradually increases, in agreement with the characteristic of oxidative addition.

In intermediate **14**, there exists a β-agostic interaction between nickel(II) with the newly formed C(sp^3)–H bond. Prior to the following C–C reductive elimination, cleavage of the β-agostic interaction is required. From **14** to **15**, the agostic interaction is transferred from C–H bond toward P–H bond, which is exergonic by 6.5 kcal mol^{-1}. Intermediate **15** then undergoes irreversible reductive elimination *via* **TS8** to form the C–C bond, generating the stable product-coordinated complex **16**. The reductive elimination barrier is only 1.0 kcal mol^{-1} higher than that of LLHT (**TS8** *versus* **TS7**). The rate-determining reductive elimination step is in good agreement with the experimentally-observed kinetic isotope effect (KIE) of $k_H/k_D \approx 1.1$. Finally, the catalytic cycle was completed by ligand exchange between complex **16** and the substrate to liberate the desired product **2a** and regenerate **c3**. Compared to the results of the OA pathway, the nickel(0)-promoted hydroarylation *via* the LLHT mechanism is much more favorable, which is consistent with previous results reported by Zhang on the Ni^0/*N*-heterocyclic carbene-catalyzed C–H cyclization of pyridines with alkenes.[11c]

The reaction pathways for the formation of the other enantiomer of product are provided in Fig. S9 and S10.† Our calculations reveal that the LLHT transition state **TS7′** leading to the (*S*)-product is 4.1 kcal mol^{-1} higher in energy than **TS7** leading to the (*R*)-product (Fig. 8). Interestingly, in the pathway of the formation of (*S*)-product, the reductive elimination (**TS8′** in Fig. S9†) becomes more facile and the LLHT is the rate-determining step. Finally, the overall barrier difference between the two competing pathways is 3.1 kcal mol^{-1}, which results in a calculated enantiomeric ratio of 99 : 1 at 95 °C. This result is consistent with the experimentally observed ratio of 96 : 4.

A new type of σ-CAM mechanism

In the new σ-CAM mechanism, the σ-coordinated complex **c1** first undergoes stepwise hydrogen transfer from the JoSPOphos to the alkene *via* the P–H oxidative addition/migratory

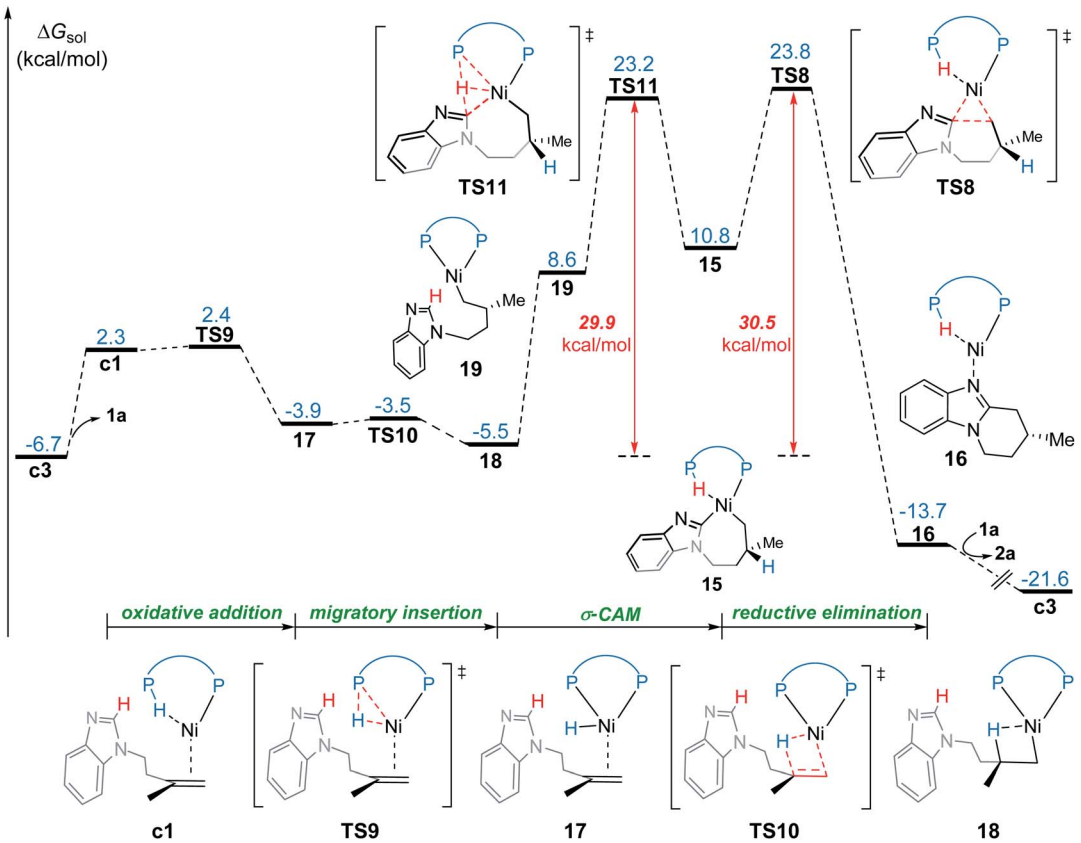

Fig. 9 Free energy profile for nickel(0)-promoted hydroarylation *via* the σ-CAM mechanism.

insertion, generating the agostic intermediate **18** (Fig. 9). The **c1** → **17** → **18** transformation is very facile, with a fairly low energy barrier. Interestingly, this process is rather similar to the migration of hydrogen to a cod ligand during the chain walking process in Fig. S2,† which indicates that this type of stepwise hydrogen transfer may be universal in the nickel(0)/JoSPOphos-catalyzed reactions that involve alkene or alkyne substrates. Rotation of the newly formed Ni–C bond in **18** results in the three-coordinate complex **19**, which then undergoes σ-CAM *via* **TS11** to generate the nickelacycle intermediate **15**. During this process, the hydrogen transfers from C(sp^2)–H to the P(v) atom of JoSPOphos. Although the behavior of hydrogen transfer in σ-CAM transition state **TS11** is similar to that in the LLHT transition state **TS7**, the changes in the formal oxidation state of Ni are obviously different. The metal is oxidized from Ni(0) to Ni(II) after the LLHT, while the formal oxidation state of Ni remains unchanged after the σ-CAM. To further illustrate this difference, we performed LOL and NPA calculations on **TS11**. As shown in Fig. 10, the LOL map clearly demonstrates the characteristic of the forming Ni–C and P–H bonds. In contrast to the results of LLHT (Fig. 7), the NPA charge of Ni remains almost constant during the σ-CAM, while the charge of the transferring H gradually decreases along the intrinsic reaction coordinates and becomes negative in intermediate **15**. From intermediate **15**, the subsequent elementary steps are the same with those in the LLHT mechanism. When comparing the two different modes of C–H activation in Fig. 6 and 9, the energy difference between the two transition states (**TS7** *versus* **TS11**) is only 0.4 kcal mol^{-1}, indicating the LLHT mechanism and the new σ-CAM mechanism both being favorable under the experimental conditions.

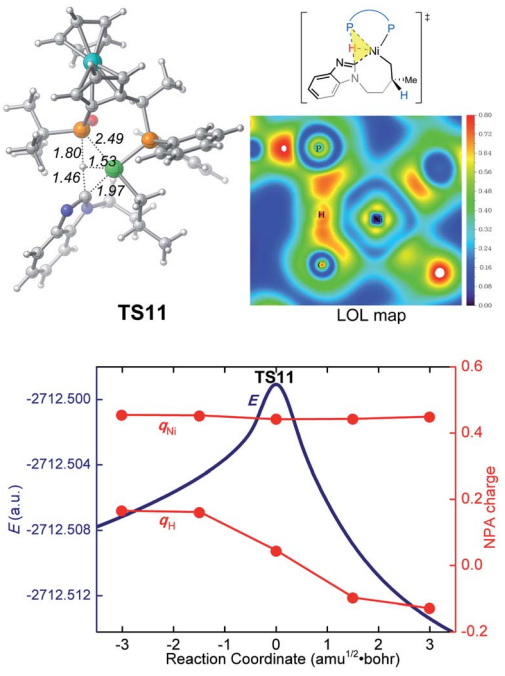

Fig. 10 Optimized structure of TS11 with selected bond distances in Å, the LOL map and the electronic energies (*E*) and NPA charges (*q*) along the intrinsic reaction coordinates.

On the basis of the above results of nickel(0)-catalyzed hydroarylation *via* the new σ-CAM mechanism, the coordination of alkene with nickel(0) through the Re- or Si-face and the subsequent migratory insertion of alkene into the Ni–H bond lead to the overall enantioselectivity. The insertion by the Re- or Si-face and the following σ-CAM and reductive elimination will lead to final (*R*)- or (*S*)-product, respectively (Fig. 11a and b). The free energy profile for the competing pathway that results in the (*S*)-product is given in Fig. S11.† Our calculated results reveal that the stepwise hydrogen transfer during the formation of (*S*)-product is also very facile. Finally, the enantiomeric ratio is determined by the rate-determining reductive elimination. The reductive elimination transition state **TS8″** leading to the (*S*)-product is 2.3 kcal mol^{-1} less stable than **TS8** leading to the (*R*)-product (Fig. 11b). This activation energy difference corresponds to a calculated enantiomeric ratio of 96 : 4 at 95 °C. This result agrees indeed well with the experimentally observed ratio of 96 : 4.[7]

In experiment, introducing different substituents on the two P atoms of JoSPOphos were found to affect the enantiomeric ratio, which highlights the importance of the interactions between the ligand and the substrate. To further understand the origins of the enantioselectivity, we examined the optimized structures of the two key reductive elimination transition states (Fig. 11c). A remarkable structural difference between **TS8** and **TS8″** represents the orientation of dimethylene group in the substrates. In **TS8**, the dimethylene group points away from JoSPOphos, thus small steric repulsions are expected between the ligand and the substrate. In contrast, in the unfavorable **TS8″**, the dimethylene motif points towards the ligand, resulting in relatively stronger steric repulsions between methylene group of the substrate and the bulky phenyl group in the ligand, as manifested by the shorter H···H distance (2.20 Å). Therefore, the more significant ligand-substrate steric repulsions in **TS8″** contribute to its relatively higher energy, eventually leading to the observed enantioselectivity.

Overall mechanism of the nickel-catalyzed hydroarylation

Our calculations reveal that the most favorable pathway involves the nickel(0) catalyst, while the nickel(II)-promoted reaction is not operative due to the significantly higher barrier of the last σ-CAM step (Fig. 1). This result prompted us to perform further experimental mechanistic investigations into the observed catalytic activity of the π-allyl nickel(II) complex **3**. To this end, careful gas chromatographic GC-FID analysis of the solution resulting from the stoichiometric reaction between complexes **3** and **1a** demonstrated the formation of 1,3-cyclooctadiene (1,3-cod) at the end of catalysis (Fig. S12†). On the basis of this experimental observation, a mechanism of the regeneration of nickel(0) catalyst **c3** from nickel(II) complex **3** is proposed and shown in Fig. 12. The π-allyl nickel(II) complex **3** first isomerizes to the unstable agostic intermediate **20** that subsequently undergoes facile β-hydride elimination/reductive elimination to form the 1,3-cod-coordinated nickel(0) complex **22**. From the thus-formed complex **22**, ligand exchange with the substrate **1a** regenerates the nickel(0) catalyst.

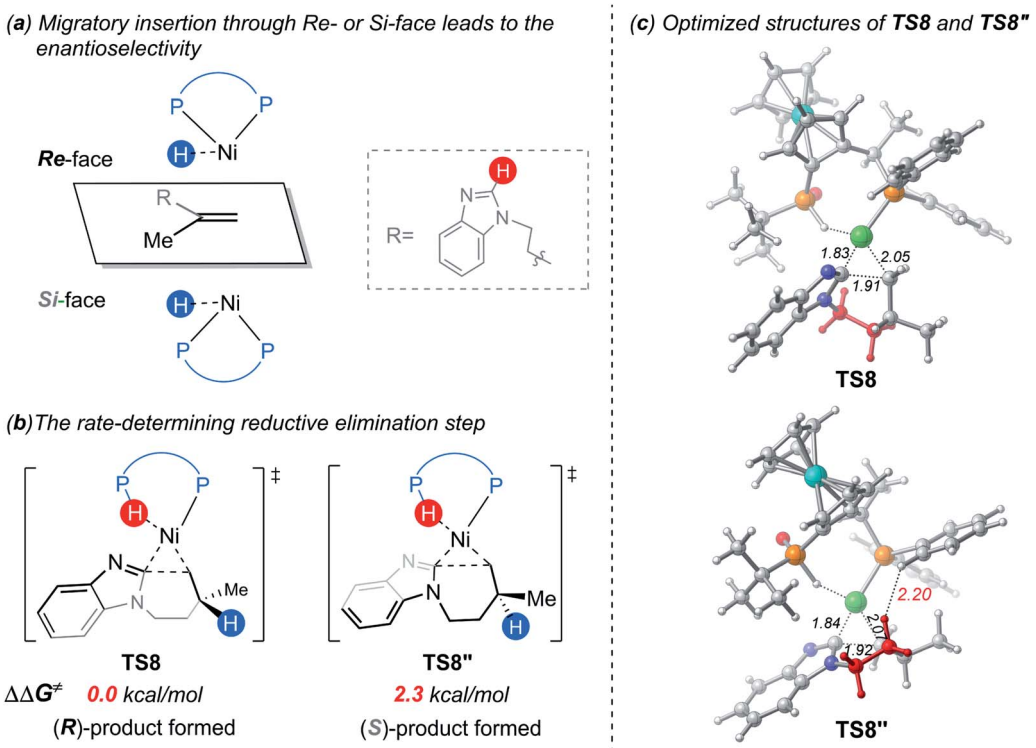

Fig. 11 (a) Migratory insertion by the Re- or Si-face of the substrate; (b) the two competing reductive elimination transition states; (c) the optimized structures of TS8 and TS8″ with selected bond distances in Å.

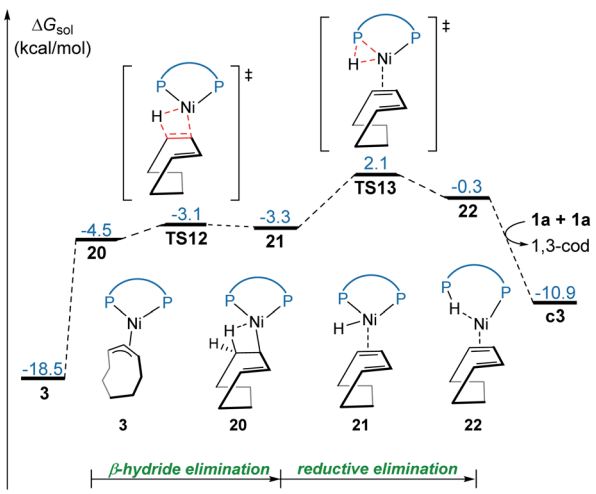

Fig. 12 Free energy profile for the regeneration of the nickel(0) catalyst from **3**.

On the basis of the above mechanistic studies, the overall mechanism of Ni-catalyzed hydroarylation is summarized in Scheme 4. From the precatalyst $Ni(cod)_2$, the ligand exchange generates the agostic complex **4**. Further ligand-substrate exchange delivers the bisligated complex **c3**. From the catalyst **c3**, there exist two favorable mechanistic pathways to generate the nickelacycle intermediate **B**. In Path a, intermediate **B** is generated by the widely proposed LLHT mechanism. In Path b, facile P–H oxidative addition and migratory insertion occur to form the agostic nickel(II) intermediate **A**. Subsequently, a new type of σ-CAM occurs to generate intermediate **B**. Finally, the rate-determining C–C reductive elimination proceeds irreversibly to yield the final hydroarylation product.

From complex **4**, a competing cod-mediated pathway can occur (Path c), ultimately resulting in the formation of the off-cycle π-allyl nickel(II) complex **3**. The formation of **3** occurs *via* traditional chain walking mechanism, and is highly exergonic. Our calculations reveal that the π-allyl complex **3** is not the active catalyst. Through a sequential β-hydride elimination/reductive elimination, the catalyst resting state **c3** is regenerated to initiate the product-forming pathway. Experimental mechanistic investigations provide additional support for this proposed mechanistic rationale. Furthermore, the overall mechanism indicates that increase in the amount of free cod ligand will facilitate the formation of off-cycle resting state **3** and impede reactivity of nickel(0) catalyst, which is consistent with the experimental observation that addition of free cod resulted in a deceleration of catalysis.

Concerning the reactivity of nickel catalysts, the relatively lower reduction potential and electronegativity leads to facile oxidative addition of nickel(0). Our computational results further disclose several unique reactivity patterns of the combination of nickel with JoSPOphos during the C–H activation with hydroarylation of alkenes (Scheme 5). The SPO can coordinate to nickel *via* an agostic interaction between P–H bond and the metal center, which is a somewhat more stable than the commonly proposed *O*-coordination. A facile hydrogen

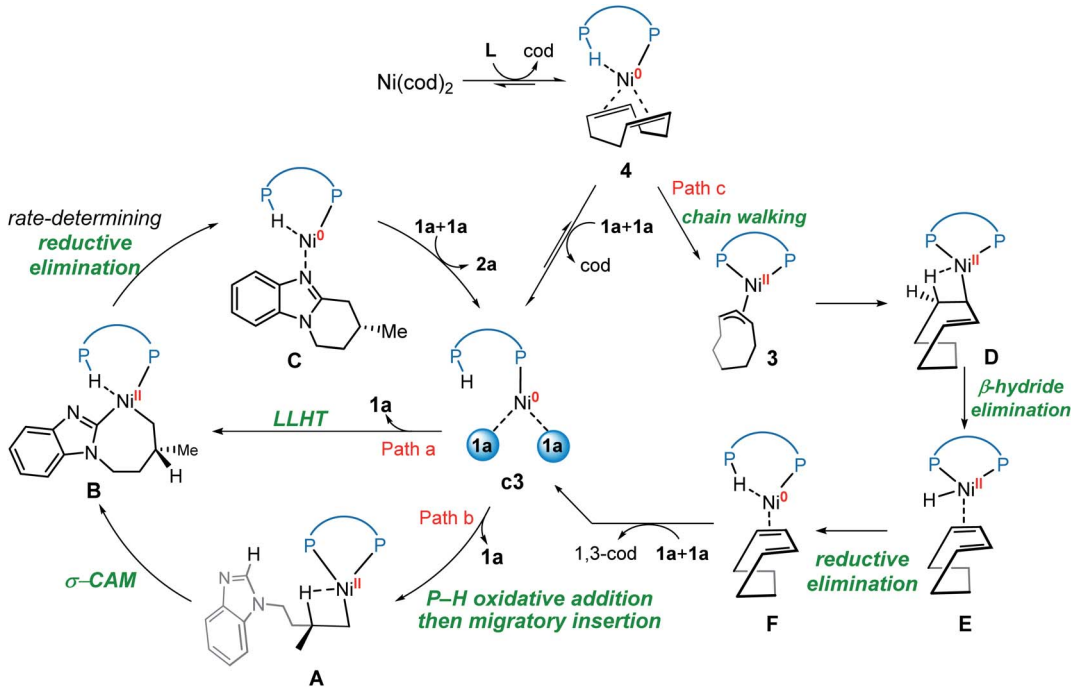

Scheme 4 Overall mechanism of the nickel-catalyzed hydroarylation.

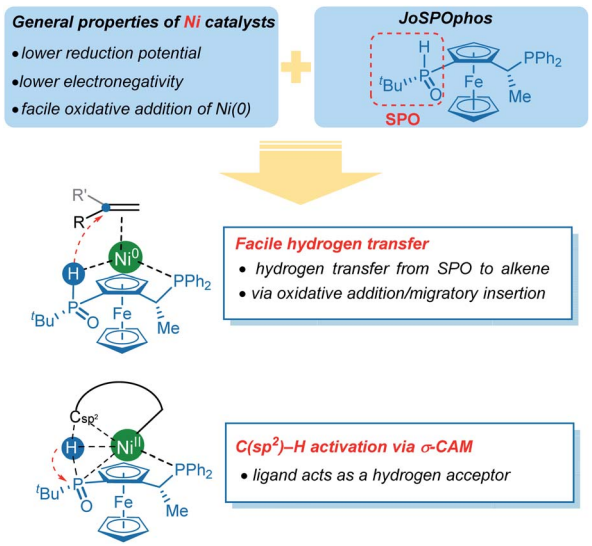

Scheme 5 Summary of the reactivity of nickel/JoSPOphos catalytic system.

transfer between the SPO and the alkene through either a two-step P–H oxidative addition and migratory insertion or a concerted reverse LLHT (Fig. S5†) is observed for the nickel/JoSPOphos catalysis manifold. This reactivity mode is largely due to the relatively weak P–H bond and a facile oxidative addition at nickel(0). This manifold is expected to be facile for alkyne substrates likewise. Interestingly, the anion of SPO can function as a hydrogen acceptor, thus promoting the C(sp^2)–H activation *via* an unconventional σ-CAM mechanism.

Conclusions

In summary, the reaction mechanisms and origins of enantioselectivity of Ni-catalyzed intramolecular C–H cyclization of imidazoles were investigated by using DFT calculations. The calculations establish that the resting state of the catalyst is the nickel(0) complex rather than a π-allyl nickel(II) complex. In addition to the typically accepted LLHT/reductive elimination pathway, an unexpected nickel(0)/nickel(II) catalytic cycle comprising P–H oxidative addition, migratory insertion, C(sp^2)–H activation *via* σ-CAM, and C–C reductive elimination is also favorable. Importantly, our computational results based on this new type of σ-CAM mechanism can reproduce rather well the experimentally observed enantioselectivity. In this new mechanism, the enantiomeric ratio is ultimately determined by the rate-determining reductive elimination steps. The different steric repulsions between methylene of the substrate and the methyl and phenyl groups of JoSPOphos ligand are responsible for the selectivity. Our calculations also show that the catalytic cycle initiated by the π-allyl nickel(II) complex is disfavored. The nickel(II) complex can be converted into the on-cycle nickel(0) complex *via* a sequential β-hydride elimination/reductive elimination, which was confirmed by experimental studies.

The combined computational and experimental results provide a deeper understanding of the Ni-catalyzed enantioselective C–H cyclization, including the significant roles of the SPO unit in JoSPOphos. The SPO facilitates the coordination with the metal center *via* agostic interaction and the occurrence of hydrogen transfer and σ-CAM steps over the course of the reaction. We anticipate that this improved understanding will help to expand the scope of application of the nickel/JoSPOphos

manifold, and provide further insights for the development of novel enantioselective C–H transformations.

Conflicts of interest

There are no conflicts to declare.

Acknowledgements

Financial support from Natural Science Foundation of Shandong Province (ZR2019YQ11), the DFG (SPP 1807), and National Natural Science Foundation of China (NSFC No. 21601110) are gratefully acknowledged.

Notes and references

1 For selected reviews on C–H activation, see: (*a*) J. C. K. Chu and T. Rovis, *Angew. Chem., Int. Ed.*, 2018, **57**, 62–101; (*b*) P. Gandeepan and L. Ackermann, *Chem*, 2018, **4**, 199–222; (*c*) Y. Park, Y. Kim and S. Chang, *Chem. Rev.*, 2017, **117**, 9247–9301; (*d*) J. He, M. Wasa, K. S. L. Chan, Q. Shao and J. Q. Yu, *Chem. Rev.*, 2017, **117**, 8754–8786; (*e*) O. Eisenstein, J. Milani and R. N. Perutz, *Chem. Rev.*, 2017, **13**, 8710–8753; (*f*) T. Gensch, M. N. Hopkinson, F. Glorius and J. Wencel-Delord, *Chem. Soc. Rev.*, 2016, **45**, 2900–2936; (*g*) Q. Zheng and N. Jiao, *Chem. Soc. Rev.*, 2016, **45**, 4590–4627; (*h*) O. Daugulis, J. Roane and L. D. Tran, *Acc. Chem. Res.*, 2015, **48**, 1053–1064; (*i*) G. Rouquet and N. Chatani, *Angew. Chem., Int. Ed.*, 2013, **52**, 11726–11743.

2 (*a*) K. D. Vogiatzis, M. V. Polynski, J. K. Kirkland, J. Townsend, A. Hashemi, C. Liu and E. A. Pidko, *Chem. Rev.*, 2019, **119**, 2453–2523; (*b*) P. Gandeepan, T. Müller, D. Zell, G. Cera, S. Warratz and L. Ackermann, *Chem. Rev.*, 2019, **119**, 2192–2452; (*c*) Y. Hu, B. Zhou and C. Wang, *Acc. Chem. Res.*, 2018, **51**, 816–827; (*d*) W. Liu and L. Ackermann, *ACS Catal.*, 2016, **6**, 3743–3752.

3 (*a*) J. Diccianni, Q. Lin and T. Diao, *Acc. Chem. Res.*, 2020, **53**, 906–919; (*b*) V. P. Ananikov, *ACS Catal.*, 2015, **5**, 1964–1971.

4 (*a*) J. Loup, U. Dhawa, F. Pesciaioli, J. Wencel-Delord and L. Ackermann, *Angew. Chem., Int. Ed.*, 2019, **58**, 12803–12818; (*b*) L. Woźniak and N. Cramer, *Trends Chem.*, 2019, **1**, 471–484.

5 (*a*) I. Ali, M. N. Lone and H. Y. Aboul-Enein, *MedChemComm*, 2017, **8**, 1742–1773; (*b*) Z. Zhang, F. Xie, J. Jia and W. Zhang, *J. Am. Chem. Soc.*, 2010, **132**, 15939–15941.

6 Y. Wang, S. Qi, Y. Luan, X. Han, S. Wang, H. Chen and M. Ye, *J. Am. Chem. Soc.*, 2018, **140**, 5360–5364.

7 J. Loup, V. Müller, D. Ghorai and L. Ackermann, *Angew. Chem., Int. Ed.*, 2019, **58**, 1749–1753.

8 For representative examples, see: (*a*) D. Berthold and B. Breit, *Org. Lett.*, 2018, **20**, 598–601; (*b*) X. Wu, Z. Chen, Y. Bai and V. M. Dong, *J. Am. Chem. Soc.*, 2016, **138**, 12013–12016; (*c*) A. M. Haydl, K. Xu and B. Breit, *Angew. Chem., Int. Ed.*, 2015, **54**, 7149–7153; (*d*) H. Landert, F. Spindler, A. Wyss, H. Blaser, B. Pugin, Y. Ribourduoille, B. Gschwend, B. Ramalingam and A. Pfaltz, *Angew. Chem., Int. Ed.*, 2010, **49**, 6873–6876.

9 A. J. Nett, J. Montgomery and P. M. Zimmerman, *ACS Catal.*, 2017, **7**, 7352–7362.

10 A. J. Nett, W. Zhao, P. M. Zimmerman and J. Montgomery, *J. Am. Chem. Soc.*, 2015, **137**, 7636–7639.

11 (*a*) H. Shao, Y. Wang, C. W. Bielawski and P. Liu, *ACS Catal.*, 2020, **10**, 3820–3827; (*b*) T. Sergeieva, T. A. Hamlin, S. Okovytyy, B. Breit and F. M. Bickelhaupt, *Chem.–Eur. J.*, 2020, **26**, 2342–2348; (*c*) X. Zhao, X. Ma, R. Zhu and D. Zhang, *Chem.–Eur. J.*, 2020, **26**, 5459–5468; (*d*) Y. Lang, M. Zhang, Y. Cao and G. Huang, *Chem. Commun.*, 2018, **54**, 2678–2681; (*e*) M. Zhang, L. Hu, Y. Lang, Y. Cao and G. Huang, *J. Org. Chem.*, 2018, **83**, 2937–2947; (*f*) G. Huang and P. Liu, *ACS Catal.*, 2016, **6**, 809–820.

12 For selected reviews on the mechanisms of C–H activation, see: (*a*) D. L. Davies, S. A. Macgregor and C. L. McMullin, *Chem. Rev.*, 2017, **117**, 8649–8709; (*b*) T. Sperger, I. A. Sanhueza, I. Kalvet and F. Schoenebeck, *Chem. Rev.*, 2015, **115**, 9532–9586; (*c*) D. Balcells, E. Clot and O. Eisenstein, *Chem. Rev.*, 2010, **110**, 749–823; (*d*) L. Ackermann, *Chem. Rev.*, 2011, **111**, 1315–1345; (*e*) D. Lapointe and K. Fagnou, *Chem. Lett.*, 2010, **39**, 1118–1126.

13 R. N. Perutz and S. Sabo-Etienne, *Angew. Chem., Int. Ed.*, 2007, **46**, 2578–2592.

14 J. Guihaumé, S. Halbert, O. Eisenstein and R. N. Perutz, *Organometallics*, 2012, **31**, 1300–1314.

15 (*a*) C. Lee, W. Yang and R. G. Parr, *Phys. Rev. B: Condens. Matter Mater. Phys.*, 1988, **37**, 785–789; (*b*) A. D. Becke, *J. Chem. Phys.*, 1993, **98**, 5648–5652.

16 S. Grimme, J. Antony, S. Ehrlich and H. Krieg, *J. Chem. Phys.*, 2010, **132**, 154104.

17 P. J. Hay and W. R. Wadt, *J. Chem. Phys.*, 1985, **82**, 299–310.

18 (*a*) H. M. Omer and P. Liu, *J. Am. Chem. Soc.*, 2017, **139**, 9909–9920; (*b*) C. Ji and X. Hong, *J. Am. Chem. Soc.*, 2017, **139**, 15522–15529; (*c*) S. Zhang, B. L. H. Taylor, C. Ji, Y. Gao, M. R. Harris, L. E. Hanna, E. R. Jarvo, K. N. Houk and X. Hong, *J. Am. Chem. Soc.*, 2017, **139**, 12994–13005.

19 S. Grimme, *Chem.–Eur. J.*, 2012, **18**, 9955–9964.

20 M. Mammen, E. I. Shakhnovich, J. M. Deutch and G. M. Whitesides, *J. Org. Chem.*, 1998, **63**, 3821–3830.

21 G. Luchini, J. V. Alegre-Requena, I. Funes-Ardoiz and R. S. Paton, *F1000Research*, 2020, **9**, 291.

22 (*a*) F. Weigend and R. Ahlrichs, *Phys. Chem. Chem. Phys.*, 2005, **7**, 3297–3305; (*b*) F. Weigend, *Phys. Chem. Chem. Phys.*, 2006, **8**, 1057–1065.

23 A. V. Marenich, C. J. Cramer and D. G. Truhlar, *J. Phys. Chem. B*, 2009, **113**, 6378–6396.

24 M. J. Frisch, G. W. Trucks, H. B. Schlegel, G. E. Scuseria, M. A. Robb, J. R. Cheeseman, G. Scalmani, V. Barone, B. Mennucci, G. A. Petersson, H. Nakatsuji, M. Caricato, X. Li, H. P. Hratchian, A. F. Izmaylov, J. Bloino, G. Zheng, J. L. Sonnenberg, M. Hada, M. Ehara, K. Toyota, R. Fukuda, J. Hasegawa, M. Ishida, T. Nakajima, Y. Honda, O. Kitao, H. Nakai, T. Vreven, J. A. Montgomery Jr, J. E. Peralta, F. Ogliaro, M. Bearpark, J. J. Heyd, E. Brothers, K. N. Kudin, V. N. Staroverov, R. Kobayashi, J. Normand, K. Raghavachari, A. Rendell, J. C. Burant, S. S. Iyengar, J. Tomasi, M. Cossi, N. Rega, J. M. Millam,

M. Klene, J. E. Knox, J. B. Cross, V. Bakken, C. Adamo, J. Jaramillo, R. Gomperts, R. E. Stratmann, O. Yazyev, A. J. Austin, R. Cammi, C. Pomelli, J. W. Ochterski, R. L. Martin, K. Morokuma, V. G. Zakrzewski, G. A. Voth, P. Salvador, J. J. Dannenberg, S. Dapprich, A. D. Daniels, Ö. Farkas, J. B. Foresman, J. V. Ortiz, J. Cioslowski and D. J. Fox, *Gaussian 09 (Revision D.01)*, Gaussian, Inc., Wallingford CT, 2009.

25 E. D. Glendening, J. K. Badenhoop, A. E. Reed, J. E. Carpenter, J. A. Bohmann, C. M. Morales and F. Weinhold, *GenNBO 5.0*, Theoretical Chemistry Institute, University of Wisconsin, Madison, 2001.

26 T. Lu and F. Chen, *J. Comput. Chem.*, 2012, **33**, 580–592.

27 C. Y. Legault, *CYLview, 1.0b*, Université de Sherbrooke, Canada, 2009, http://www.cylview.org.

28 (*a*) A. Christiansen, C. Li, M. Garland, D. Selent, R. Ludwig, A. Spannenberg, W. Baumann, R. Franke and A. Börner, *Eur. J. Org. Chem.*, 2010, **2010**, 2733–2741; (*b*) L. Ackermann, *Isr. J. Chem.*, 2010, **50**, 652–663; (*c*) L. Ackermann, *Synthesis*, 2006, 1557–1571.

29 R. F. W. Bader, *Chem. Rev.*, 1991, **91**, 893–928.

30 We also considered the possibility of the direct formation of intermediate **15** through a transition state by keeping P–H agostic interaction intact. However, we failed to locate the corresponding LLHT transition state due to the steric repulsions between SPO and the benzoimidazolyl.

31 Similar transition states have been previously reported for other transition-metal catalysts, see: (*a*) S. Ding, L. Song, Y. Wang, X. Zhang, L. W. Chung, Y. Wu and J. Sun, *Angew. Chem., Int. Ed.*, 2015, **54**, 5632–5635; (*b*) L. Song, S. Ding, Y. Wang, X. Zhang, Y. Wu and J. Sun, *J. Org. Chem.*, 2016, **81**, 6157–6164; (*c*) B. E. Haines, Y. Saito, Y. Segawa, K. Itami and D. G. Musaev, *ACS Catal.*, 2016, **6**, 7536–7546.

32 X.-J. Liu, Y. Tian, H. Cui and H. Fan, *Chem. Commun.*, 2018, **54**, 7912–7915.